

Optical fields spanning the 4D space of nonparaxial polarization

David Marco^{1, 2} and Miguel A. Alonso^{1, 3, 4, 5}

¹ Aix Marseille Univ., CNRS, Centrale Marseille, Institut Fresnel, UMR 7249, 13397 Marseille Cedex 20, France

² Instituto de Bioingeniería, Universidad Miguel Hernández de Elche, 03202 Elche, Spain

³ The Institute of Optics, University of Rochester, Rochester, NY14627, USA

⁴ Center for Coherence and Quantum Optics, University of Rochester, Rochester, NY14627, USA

⁵ Laboratory for Laser Energetics, University of Rochester, Rochester, NY14627, USA

E-mails: david.marco@fresnel.fr, miguel.alonso@fresnel.fr

December 5, 2022

Abstract

We present simple mathematical solutions for optical fields that span all nonparaxial polarization ellipses. These fields, given by a superposition of five plane waves with non-coplanar polarizations, are experimentally realizable. By slowly varying in time the relative amplitude between two groups of plane waves, the resulting fields take the form of a periodic polarization lattice, where all possible nonparaxial polarization ellipses are localized in a 4D spatio-temporal cell. The field distributions in these cells can be regarded as 4D skyrmionic textures.

1 Introduction

For a monochromatic optical field, the electric field vector at any given point traces in time an ellipse [1]. The parameters that describe the shape and orientation of this ellipse (other than its size, which is related to the field's intensity) are what we call polarization. For a monochromatic paraxial optical field, the ellipse is essentially constrained to the plane perpendicular to the main direction of propagation, so only two parameters are required to describe polarization: the ellipticity and the orientation angle within the plane. These two quantities are well represented by the two coordinates over the surface of a unit sphere known as the Poincaré sphere. Polarization can change from point to point across (or along) a beam. Since the Poincaré sphere is a 2D abstract space, it is possible for a beam to contain many or even all polarization states at a given physical plane transverse to its main direction of propagation. Simple solutions such as the so-called full Poincaré beams [2] contain all polarization states at each transverse plane. For these beams, the Poincaré sphere is mapped onto the plane according to a stereographic projection. Since the sphere is covered entirely without any singularities of the mapping (except at infinity), this field can be regarded as a 2D *skyrmionic* structure. Skyrmions correspond to topological structures in which a closed abstract parameter space (the Poincaré sphere in this case) is mapped completely and monotonically onto the flat physical space. They have been studied in several areas of physics, especially in magnetic systems [3].

For monochromatic nonparaxial fields, the plane containing the polarization ellipse at any given point is not fixed by the main direction of propagation. Four parameters are then required to fully describe polarization, such as the ellipticity and the three Euler angles determining the orientation of the ellipse. These parameters define then a 4D space of nonparaxial polarization, for which several geometric representations have been proposed in terms of two points over the surface of a unit sphere [4, 5, 6]. For a nonparaxial field, polarization typically changes from point to point. However, the 3D physical space is not sufficient to fully explore the 4D polarization space, unless it is supplemented with a fourth dimension, such as time.

Here we present what we refer to for brevity as *full 3D polarization (F3DP) fields*, which are nonparaxial optical fields containing all possible polarization ellipses. We describe a family of experimentally realizable mathematical solutions of such fields in the form of optical lattices whose polarization state changes not only in 3D space but also adiabatically in time, so that all possible nonparaxial

polarization ellipses exist inside a cuboid in 3D space within a given temporal interval. The fields are constructed as superpositions of five noncoplanar plane waves. The adiabatic temporal variation of these quasimonochromatic fields is implemented by slowly varying the relative amplitude between two sets of plane waves. Some of the solutions present uniform intensity in space and time, and they all present a rich polarization structure. These field can be experimentally implemented in the focal region of a high numerical aperture lens.

Moreover, we identified 4D skyrmionic structures in these F3DP fields. Most skyrmionic structures studied so far in vector waves are 2D skyrmions (also known as *baby skyrmions*), which fully span at a plane or a section of a plane a spherical space corresponding to an aspect of the polarization ellipse, such as: the normalized Stokes vector for paraxial beams [2, 7, 8]; the direction of the field vector at a fixed time for the electromagnetic evanescent waves of surface plasmon polaritons [9], evanescent acoustic waves [10] and traveling acoustic waves [11]; the direction of the spin vector (normal to the ellipse) in evanescent optical fields [12] and at the focal plane of tightly focused optical fields [13]; and the direction of the ellipse major axis for tightly focused optical fields [13]. Recently, a 3D skyrmionic Hopfion was found in the propagating volume of a paraxial field [14], which spans a 3-sphere where every 2D polarization state with any global phase is represented. To study the 4D skyrmionic structures within F3DP fields, we define a Skyrme density as the Jacobian of the mapping between the coordinates over the unit sphere of two points representing nonparaxial polarization states and the flat space-time. The integral of this density over a skyrmionic spatiotemporal cell is shown to give a Skyrme number of unit size.

2 Constructing the optical field

In this section, we propose a temporally-variant quasi-monochromatic field that contains all possible states of full polarization within a spatio-temporal cell with spatial dimensions of the order of a wavelength. This field consists of a simple combination of five plane waves. By changing the angles between these plane waves the field can be made more directional, and the cell containing all polarization states can be made larger.

2.1 The construction and laboratory reference frames

At any given point the complex electric vector \mathbf{E} of a nonparaxial (quasi)monochromatic field can be expressed as

$$\mathbf{E} = A \exp(i\Phi) \left[\sin \gamma_1 (\mathbf{x} \cos \gamma_2 e^{-i\delta_1} + \mathbf{z} \sin \gamma_2 e^{-i\delta_2}) + \mathbf{y} \cos \gamma_1 \right], \quad (1)$$

where \mathbf{x} , \mathbf{y} and \mathbf{z} are unit vectors in the x , y and z directions, respectively, and the six real parameters $A, \Phi, \gamma_1, \gamma_2, \delta_1, \delta_2$ are functions of position, and even time as long as their variation is negligible over the scale of an optical cycle. The real electric field is obtained by taking the real part of $\mathbf{E} \exp(-i\omega t)$, where ω is the carrier temporal angular frequency of oscillation. Note that only four parameters are required to describe a 3D polarization state, since the global amplitude A and the global phase Φ do not affect the shape and orientation of the ellipse traced by the electric field over a temporal period. In order for the field to span all polarization states, these four parameters must span a range of values, for example: $0 \leq \gamma_1, \gamma_2 \leq \pi/2$, which account for all relative amplitudes between the three field components, and $0 \leq \delta_1, \delta_2 < 2\pi$, which account for all relative phases. Therefore, in order to design a field that covers all states of polarization, we must map the complete abstract four-parameter space $(\gamma_1, \gamma_2, \delta_1, \delta_2)$ onto the physical space-time (x, y, z, t) , with the constraint that the field must be a solution of Maxwell's equations in free space. Under the approximation that the temporal dependence of the polarization parameters is much slower than the scale set by ω , these conditions reduce to requiring the form in Eq. (1) to satisfy the Helmholtz equation and to have zero divergence.

It turns out that a simple solution can be found by making two assumptions: i) the global amplitude A is constant and hence can be set to unity, and ii) each of the four polarization parameters depends linearly on one of the spatio-temporal coordinates. The following combination, for example, achieves the desired goals: $\gamma_2 \rightarrow ky/\sqrt{2}$, $\delta_1 \rightarrow kx/\sqrt{2}$, $\delta_2 \rightarrow kz/\sqrt{2}$, where $k = \omega/c = 2\pi/\lambda$ is the wavenumber with λ being the wavelength, and $\gamma_1 \rightarrow \Omega t$, where $\Omega \ll \omega$. By also letting $\Phi = k(x+z)/\sqrt{2}$ we arrive

at the normalized field

$$\begin{aligned} \mathbf{E} &= \left[\sin \Omega t \left(\mathbf{x} e^{-i \frac{kx}{\sqrt{2}}} \cos \frac{ky}{\sqrt{2}} + \mathbf{z} e^{-i \frac{kz}{\sqrt{2}}} \sin \frac{ky}{\sqrt{2}} \right) + \mathbf{y} \cos \Omega t \right] e^{ik \frac{x+z}{\sqrt{2}}} \\ &= \mathbf{x} \frac{\sin \Omega t}{2} (e^{i\mathbf{k}_{xA} \cdot \mathbf{r}} + e^{i\mathbf{k}_{xB} \cdot \mathbf{r}}) + \mathbf{z} \frac{\sin \Omega t}{2i} (e^{i\mathbf{k}_{zA} \cdot \mathbf{r}} - e^{i\mathbf{k}_{zB} \cdot \mathbf{r}}) + \mathbf{y} \cos \Omega t e^{i\mathbf{k}_y \cdot \mathbf{r}}, \end{aligned} \quad (2)$$

where in the second step the y -dependent trigonometric functions were separated into complex exponentials to show that this field is a superposition of five plane waves. The amplitudes of these plane waves have a slow temporal dependence that adiabatically changes the relative weight of the first four with respect to the fifth, as depicted in Fig. 1(a). The wavevectors of these five plane waves are

$$\mathbf{k}_{xA} = k(0, 1, 1)/\sqrt{2}, \quad (3a)$$

$$\mathbf{k}_{xB} = k(0, -1, 1)/\sqrt{2}, \quad (3b)$$

$$\mathbf{k}_{zA} = k(1, 1, 0)/\sqrt{2}, \quad (3c)$$

$$\mathbf{k}_{zB} = k(1, -1, 0)/\sqrt{2}, \quad (3d)$$

$$\mathbf{k}_y = k(1, 0, 1)/\sqrt{2}, \quad (3e)$$

each being orthogonal to the polarization of the corresponding plane wave (indicated in the subindex). All nonparaxial polarization ellipses then exist inside the cuboid defined by $x, z \in [0, \sqrt{2}\lambda]$ and $y \in [0, \sqrt{2}\lambda/4]$ within a time interval $\Omega t \in [0, \pi/2]$, referred to here as a *full 3D polarization (F3DP) cell*. This spatio-temporal cell is depicted in Fig. 1(b). As mentioned earlier, while all polarization states are explored by this field, its intensity $|\mathbf{E}|^2$ is constant in space and time.

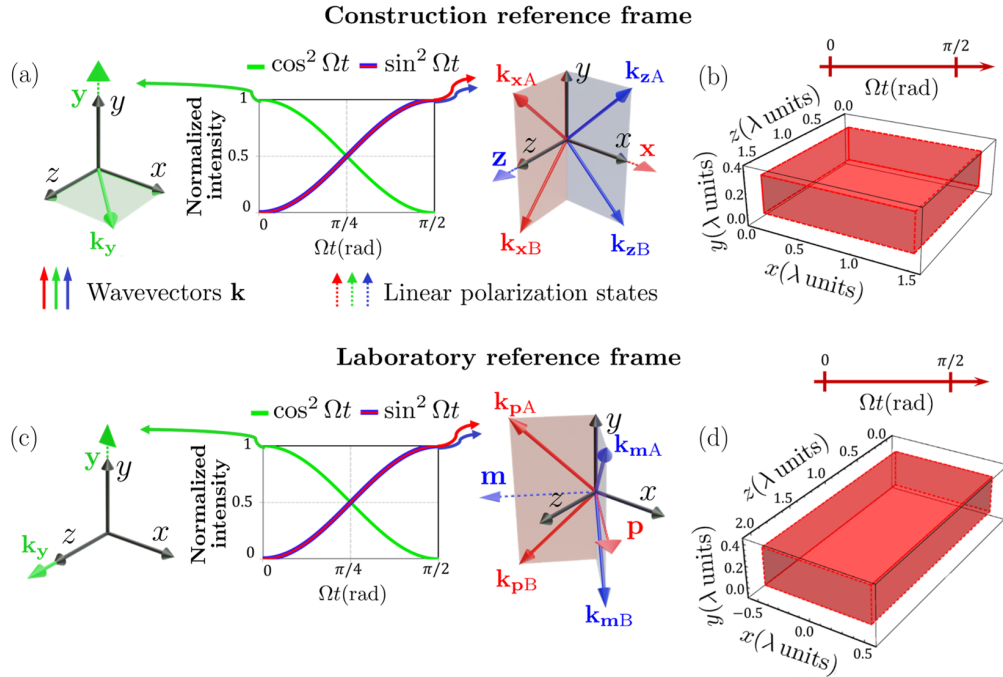


Figure 1: (a,c) Wavevectors and their polarization for five plane waves that compose a nonparaxial optical field containing all possible polarization states, in (a) the construction frame and (c) the laboratory frame. The field is constructed by adiabatically harmonically varying in time the relative amplitude between two sets of plane waves (green, and red and blue). The temporal evolution of the normalized intensity of each group of plane waves is shown. (b,d) Spatial cell where every possible nonparaxial polarization ellipse is contained within a temporal interval (F3DP cell) $\Omega t \in [0, \pi/2]$. The cells are aligned with the reference frame coordinates in the (b) construction and (d) laboratory frames.

The reference frame just used (termed here the *construction frame*) is convenient for understanding why the field spans all possible polarization states. However, we now change to a reference frame that

is better suited for visualizing the polarization structure and for describing its experimental generation. We call this new frame the *laboratory frame*, for which the z direction is chosen to coincide with the wavevector \mathbf{k}_y , which bisects the other four wavevectors and can therefore be regarded as the main propagation direction. The laboratory frame results from a rotation by $-\pi/4$ radians around the y axis of the solution in the construction frame, as shown in Fig. 1(c). Following this rotation both for the spatial coordinates and the polarization components, we arrive at the expression

$$\begin{aligned}\mathbf{E} &= \left[e^{-ik(z+x)/2} \sin \Omega t \left(\mathbf{p} \cos \frac{ky}{\sqrt{2}} + \mathbf{m} e^{ikx} \sin \frac{ky}{\sqrt{2}} \right) + \mathbf{y} \cos \Omega t \right] e^{ikz} \\ &= \mathbf{p} \frac{\sin \Omega t}{2} (e^{i\mathbf{k}_{pA} \cdot \mathbf{r}} + e^{i\mathbf{k}_{pB} \cdot \mathbf{r}}) + \mathbf{m} \frac{\sin \Omega t}{2i} (e^{i\mathbf{k}_{mA} \cdot \mathbf{r}} - e^{i\mathbf{k}_{mB} \cdot \mathbf{r}}) + \mathbf{y} \cos \Omega t e^{i\mathbf{k}_y \cdot \mathbf{r}},\end{aligned}\quad (4)$$

where the polarization components \mathbf{x} and \mathbf{z} turned into the components \mathbf{p} and \mathbf{m} , respectively, defined as

$$\mathbf{p}, \mathbf{m} = \frac{\pm \mathbf{x} + \mathbf{z}}{\sqrt{2}}, \quad (5)$$

and the corresponding wavevectors are given by

$$\mathbf{k}_{pA} = k \left(-1, \sqrt{2}, 1 \right) / 2, \quad (6a)$$

$$\mathbf{k}_{pB} = k \left(-1, -\sqrt{2}, 1 \right) / 2, \quad (6b)$$

$$\mathbf{k}_{mA} = k \left(1, \sqrt{2}, 1 \right) / 2, \quad (6c)$$

$$\mathbf{k}_{mB} = k \left(1, -\sqrt{2}, 1 \right) / 2, \quad (6d)$$

$$\mathbf{k}_y = k (0, 0, 1). \quad (6e)$$

Note that the F3DP cell in Fig. 1(b) now has sides that in the laboratory frame are at $\pm\pi/4$ with respect to the x and z axes. We then choose new F3DP cells whose boundaries are aligned with the coordinates of the laboratory frame, by considering the range that the coordinates must sweep to span all possible relative amplitudes and phases between the coefficients of \mathbf{p} , \mathbf{m} and \mathbf{y} . One such cell is given by $x \in [-\lambda/2, \lambda/2]$, $y \in [0, \sqrt{2}\lambda/4]$, and $z \in [0, 2\lambda]$, for the same time interval as before. The spatial volume of this cell is the same as for the previous one: $\lambda^3/\sqrt{2}$. This cell is depicted in Fig. 1(d).

2.2 Increasing the size of the F3DP cell

The spatial dimensions of this F3DP cell can be increased by making the field more directional, that is, by bringing the wavevectors of the four plane waves with polarization states \mathbf{p} and \mathbf{m} (red and blue in Fig. 1(c)) closer to the main propagation direction (z). It is useful to regard this transformation as a composition of the two transformations depicted in Fig. 2(a): First, a decrease of the angle 2α subtended by each pair of wavevectors with the same polarization (blue-blue and red-red pairs in Fig. 2(a)). Second, a decrease in the angle β between the projection onto the xz plane of each of these four wavevectors and the z axis (so that 2β is the angle between the projections of the blue-red pairs in Fig. 2(a)). The wavevectors then take the form

$$\mathbf{k}_{pA} = k (-\cos \alpha \sin \beta, \sin \alpha, \cos \alpha \cos \beta), \quad (7a)$$

$$\mathbf{k}_{pB} = k (-\cos \alpha \sin \beta, -\sin \alpha, \cos \alpha \cos \beta), \quad (7b)$$

$$\mathbf{k}_{mA} = k (\cos \alpha \sin \beta, \sin \alpha, \cos \alpha \cos \beta), \quad (7c)$$

$$\mathbf{k}_{mB} = k (\cos \alpha \sin \beta, -\sin \alpha, \cos \alpha \cos \beta), \quad (7d)$$

$$\mathbf{k}_y = k (0, 0, 1), \quad (7e)$$

where the particular case in Eq. (6) corresponds to $\alpha = \beta = \pi/4$. Note that if $\beta = \pi/4$ these wavevectors remain perpendicular to the corresponding polarization vectors (\mathbf{p} , \mathbf{m} , or \mathbf{y}) regardless of the value of α , and in fact the intensity of the field remains constant. However, changing to $\beta \neq \pi/4$ does require the rotation of the polarization vectors for the first four plane waves according to

$$\mathbf{p}, \mathbf{m} = \pm \mathbf{x} \cos \beta + \mathbf{z} \sin \beta, \quad (8)$$

in order to ensure plane-wave transversality. Since for $\beta \neq \pi/4$ these two polarization components are not mutually orthogonal, the intensity of the field is no longer spatio-temporally uniform. The field can now be written as

$$\begin{aligned} \mathbf{E} &= \left[e^{-i(\kappa_z z + \kappa_x x)} \sin \Omega t (\mathbf{p} \cos \kappa_y y + \mathbf{m} e^{i2\kappa_x x} \sin \kappa_y y) + \mathbf{y} \cos \Omega t \right] e^{ikz} \\ &= \mathbf{p} \frac{\sin \Omega t}{2} (e^{i\mathbf{k}_{pA} \cdot \mathbf{r}} + e^{i\mathbf{k}_{pB} \cdot \mathbf{r}}) + \mathbf{m} \frac{\sin \Omega t}{2i} (e^{i\mathbf{k}_{mA} \cdot \mathbf{r}} - e^{i\mathbf{k}_{mB} \cdot \mathbf{r}}) + \mathbf{y} \cos \Omega t e^{i\mathbf{k}_y \cdot \mathbf{r}}, \end{aligned} \quad (9)$$

where the spatial frequencies between contributions are given by

$$\kappa_x = k \cos \alpha \sin \beta, \quad (10a)$$

$$\kappa_y = k \sin \alpha, \quad (10b)$$

$$\kappa_z = k(1 - \cos \alpha \cos \beta). \quad (10c)$$

The dimensions of the F3DP cell are inversely proportional to these spatial frequencies, as shown in Fig. 2(b), and can be made in principle arbitrarily large by making the angles α and β smaller. Note that for $\beta \neq \pi/4$ the polarization vectors \mathbf{p} , \mathbf{m} and \mathbf{y} no longer define an orthogonal set, but they are still linearly independent, and all possible relative amplitudes and phases between them are swept in the cell, giving rise to all polarization states. However, for small β some polarization states are present only in regions of relatively low intensity, and their coverage becomes less uniform.

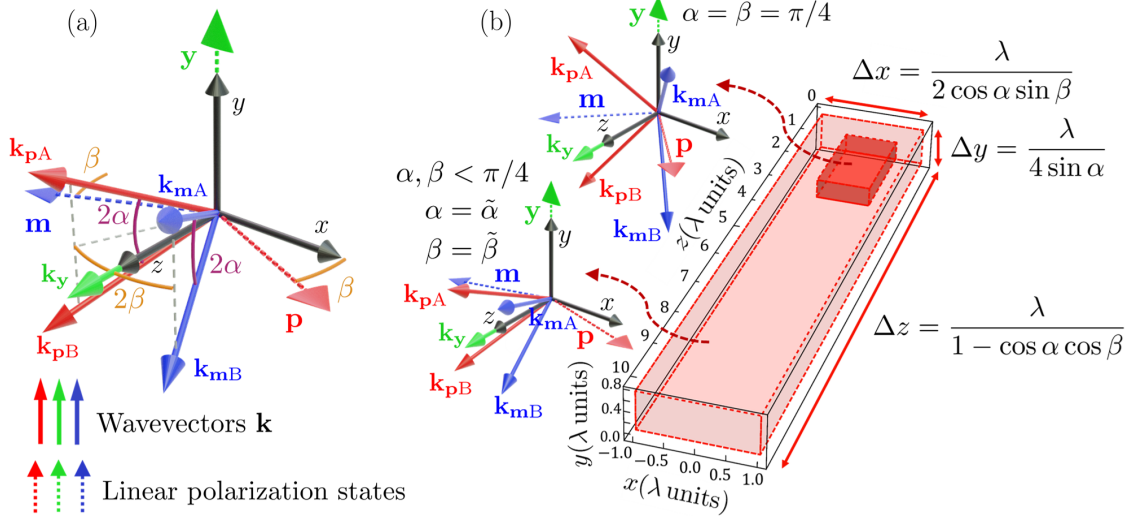


Figure 2: (a) The dimensions of the F3DP cell can be controlled by changing the angles α and β for the wavevectors and the corresponding polarization vectors. The angle between two wavevectors with the same polarization state (blue-blue or red-red pairs) is 2α , and the angle between the projections onto the xz plane of these two pairs of wavevectors (blue-red pairs) is 2β . (b) The size of the F3DP cell increases as α and β decrease: the smaller cell in the figure corresponds to $\alpha = \beta = \pi/4$, while the larger one (whose dimensions in x and y are twice those of the smaller one) corresponds to $\alpha = \tilde{\alpha} = \arcsin[1/(2\sqrt{2})] = 0.3614$ and $\beta = \tilde{\beta} = \arcsin(1/\sqrt{14}) = 0.2706$.

This field can be implemented experimentally by focusing with a microscope objective the light emerging from five points at the back focal plane, where the polarization and phase of each is appropriately prepared. The separation of the points sets the value of the angles α and β . The minimum numerical aperture (in air) required to produce this field is $(1 - \cos^2 \alpha \cos^2 \beta)^{1/2}$.

3 The polarization structure of the field

We now describe the polarization structure of the field. We start by describing the global field distribution by finding its spatial unit cell. We then study the spatio-temporal structure of polarization singularities inside a F3DP cell.

3.1 The field's global structure

Figure 3(a) depicts a unit cell of the field, which consists of two stacked F3DP cells (red and green cuboids). The cell dimensions are expressed in units of $\kappa_j j$ ($j = x, y, z$), so the representation is valid for any value of α and β . The cell A (red) is the F3DP cell described in the previous section, which can be written as $\kappa_x x \in [-\pi/2, \pi/2)$, $\kappa_y y \in [0, \pi/2]$ and $\kappa_z z \in [0, 2\pi)$. The cell B (green) is an F3DP cell displaced by $\pi/2$ in each dimensionless coordinate $\kappa_j j$ with respect to A. It turns out that the polarization distributions in A and B are identical except for a mirroring in y , as one can see from applying a shift of $\pi/2$ to $\kappa_x x$, $\kappa_y y$ and $\kappa_z z$ in Eq. (9). The entire field can then be constructed by stacking these unit cells, as shown in Figs. 3(b,c). The positions where the unit cells must be stacked are deduced from the changes in $\kappa_j j$ that leave the field in Eq. (9) invariant: i) a displacement of $n\pi$ ($n \in \mathbb{Z}$) in $\kappa_x x$ and $\kappa_z z$ (which results in the brick structure in Fig. 3(b) for each type of cell), and ii) a displacement of $n\pi$ in $\kappa_y y$ and a shift of $n\pi$ in $\kappa_x x$ or $\kappa_z z$ (depicted in Fig. 3(c)).

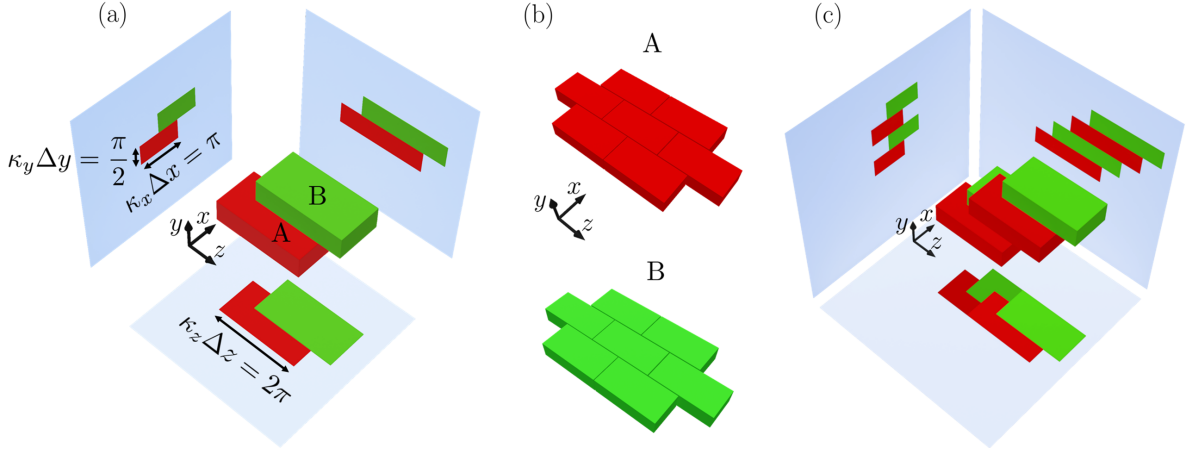


Figure 3: (a) The field unit cell consists of two F3DP cells (red and green boxes) of dimensions $\Delta x = \pi/\kappa_x = \lambda/(2 \cos \alpha \sin \beta)$, $\Delta y = \pi/(2\kappa_y) = \lambda/(4 \sin \alpha)$ and $\Delta z = 2\pi/\kappa_z = \lambda/(1 - \cos \alpha \cos \beta)$. The cell dimensions are expressed in units of $\kappa_j j$ ($j = x, y, z$). Projections onto the xy , xz and yz planes are shown in order to aid with 3D visualization. The (green) cell B is displaced by $\pi/2$ rad in $\kappa_x x$, $\kappa_y y$ and $\kappa_z z$ with respect to the (red) cell A, and its polarization state distribution is the same as in the red cell but mirrored in y . The global field structure is reproduced by stacking unit cells following two rules: stacking unit cells displaced (b) by $n\pi$ (where $n \in \mathbb{Z}$) in $\kappa_x x$ and $\kappa_z z$ (brick structure), and (c) by $n\pi$ in $\kappa_y y$ and displaced by $n\pi$ in $\kappa_x x$ or in $\kappa_z z$.

3.2 The skeleton of the polarization distribution: L-lines and C-lines

In order to gain intuition about the spatiotemporal distribution of the polarization states, we now study the L-lines (lines of linear polarization) and C-lines (lines of circular polarization) inside the F3DP cell A. Figure 4 shows the evolution of these lines for $\alpha, \beta = \pi/4$. (The corresponding polarization structure for $\alpha = \tilde{\alpha}$ and $\beta = \tilde{\beta}$ is shown in the supplementary material in section A.1.) Once we describe the polarization state distribution inside cell A, the corresponding distribution in cell B can be obtained by just mirroring in y , as mentioned earlier.

At different times this idealized field presents L-lines, L-planes and even an L-volume (the latter two being of course unstable under field perturbations). For $\Omega t = 0$, the polarization state is \mathbf{y} , so the entire 3D space is an L-volume. On the other hand, for $\Omega t = \pi/2$, the zones of linear polarization are two sets of L-planes, which are constant in x and in y , respectively. Within the interval $\Omega t \in (0, \pi/2)$, the field presents L-lines whose positions remain constant in time. A detailed explanation of the calculations of the L-lines is provided in the supplementary material in subsection A.1.1.

Figures 5(a,b) show that, for $\Omega t \in [0, \pi/2]$, the electric field orientation at the regions of linear polarization covers the complete unit sphere. Note that antipodal points correspond to the same linear polarization state. Each curve (or more correctly, each pair of curves) represents all the values of the orientation of the linearly polarized states at a given instant. These curves are independent of

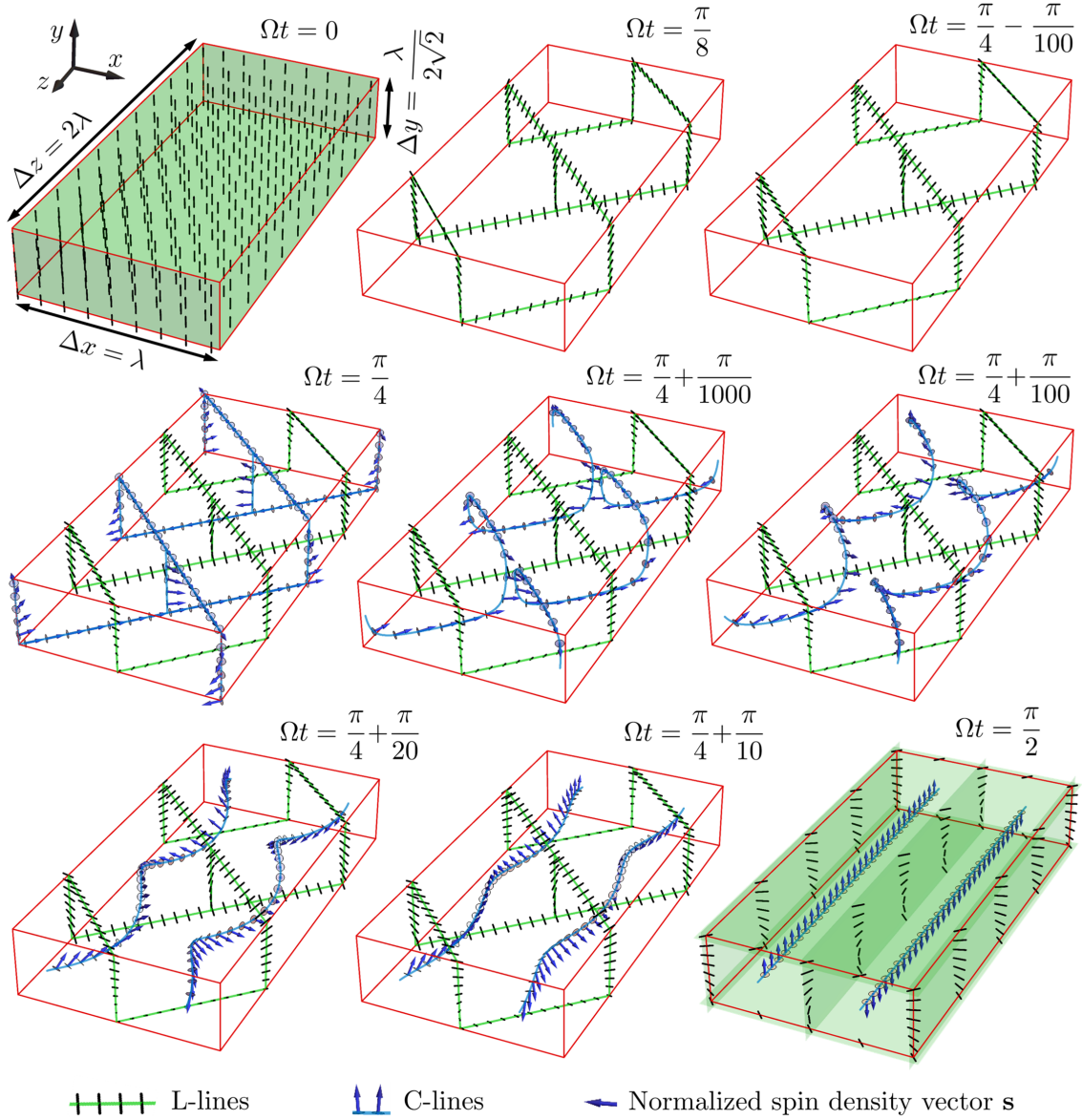


Figure 4: Temporal evolution of the L-lines and C-lines inside the F3DP cell A for $\alpha, \beta = \pi/4$.

α , and, for $\beta = \pi/4$ (Fig. 5(a)), they are parallels. Decreasing β (Fig. 5(b) for $\beta = \tilde{\beta}$) distorts the curves while maintaining full directional coverage. It is clear from Eq. (9) that, for any value of β , the \mathbf{y} polarization component of the field decreases while the \mathbf{p} and \mathbf{m} components grow. Eventually, all the polarization ellipses lie on the xz plane at $\Omega t = \pi/2$. This fact explains why, in the unit sphere in Figs. 5(a,b), the curves move from the poles towards the equator as time increases.

The C-lines are found from the constraint $\mathbf{E} \cdot \mathbf{E} = 0$ [15]. Since $\mathbf{E} \cdot \mathbf{E}$ is a complex quantity, this constraint imposes two conditions, each defining a surface, and the intersections of these surfaces are the C-lines. Figure 4 shows the normalized spin density vector $\mathbf{s} = \text{Im}(\mathbf{E}^* \times \mathbf{E})/|\mathbf{E}|^2$ along the C-lines. This vector is normal to the plane containing the ellipse, and its magnitude is proportional to the area of the normalized ellipse, ranging from 0 (linear polarization) to 1 (circular polarization). The equations describing the C-lines and \mathbf{s} are included in the supplementary material in subsection A.1.2.

There are no C-lines at $t = 0$; they appear at a time t_C , which depends only on β , and then undergo two topological transitions within the interval $\Omega t \in [0, \pi/2]$. The first transition always occurs at the time $\Omega t_{T1} = \pi/4$, and the other one occurs at Ωt_{T2} , which depends on β . The dependence of t_C and t_{T2} with β is discussed in the supplementary material. For $\beta = \pi/4$ the two topological transitions coincide with the appearance of the C-lines, $\Omega t_C = \Omega t_{T1} = \Omega t_{T2} = \pi/4$, while choosing a smaller β

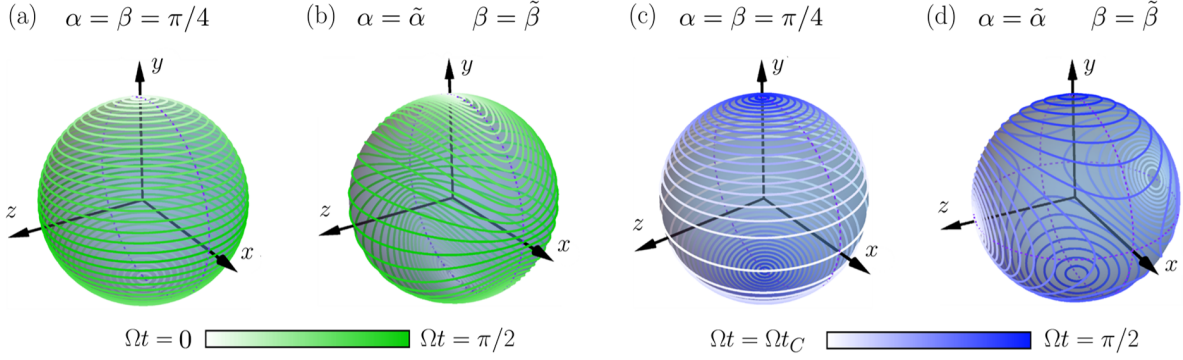


Figure 5: Temporal evolution on the unit sphere in real space of (a,b) the electric field vector direction for linearly polarized states, and (c,d) the normalized spin density vector for circularly polarized states, for (a,c) $\alpha = \beta = \pi/4$, and (b,d) $\alpha = \tilde{\alpha}$ and $\beta = \tilde{\beta}$. Each curve correspond to one temporal instant, and the spacing between temporal intervals is constant. The C-lines are plotted starting from the time t_C when they appear: $\Omega t_C = \pi/4$ for $\beta = \pi/4$ and $\Omega t_C = 0.6331$ for $\beta = \tilde{\beta}$.

causes t_C to decrease and t_{T1} to increase. Conversely, if α is reduced, the C-lines get stretched out along y and z and shrink slightly along x , but t_C and t_{T2} remain unaltered, i.e., α does not alter the topological properties of the C-lines. Studying the case when $\beta = \pi/4$ and one case when $\beta < \pi/4$ (in subsection A.1.2 in the supplementary material) is sufficient then to illustrate the topological behavior of the C-lines. Figure 4 shows the L-lines and C-lines for $\alpha = \beta = \pi/4$. Right after appearing at $\Omega t = \pi/4$ as interconnected straight lines, the C-lines split into two helices within the cell. As time increases, these helices straighten until they become parallel straight lines for $\Omega t = \pi/2$. At this time the \mathbf{y} field component vanishes, so the spin at every point is in the \mathbf{y} direction (normal to the main propagation direction), leading to “photonic wheels” with transverse spin [16, 17].

We plot the spin directions \mathbf{s} along the C-lines for a given temporal instant as a curve on the unit sphere in Figs. 5(c,d). For $\Omega t = \pi/4$, \mathbf{s} spans all directions within the xz plane for $\beta = \pi/4$ (equator of the sphere in Fig. 5(c)). After $\Omega t = \pi/4$, each of the two C-lines traces identical parallels, each on a different hemisphere: the vector \mathbf{s} at the C-line in the region $-0.5\lambda < x < 0$ ($0 < x < 0.5\lambda$) evolves in time towards the direction $+y$ ($-y$). As was the case in Figs. 5(a,b), the curves do not depend on α but they are no longer parallels for $\beta < \pi/4$ (Fig. 5(d)), while still covering all possible spin directions along the C-lines within the time interval $\Omega t \in [0, \pi/2]$. Note from Fig. 5(d) that the topological transition at t_{T2} ($\Omega t_{T2} = 1.2094$ for $\beta = \tilde{\beta}$) corresponds to topological transitions of the spin curves at $\pm x$ over the unit sphere: the curves that cycle around the z axis correspond to $t < t_{T2}$, while those that cycle around the y axis correspond to $t > t_{T2}$.

The temporal evolution of the field skeleton for $\alpha = \beta = \pi/4$ (Fig. 4) and for $\alpha = \tilde{\alpha}$, $\beta = \tilde{\beta}$ (Fig. 8) are included in the supplementary **video 1** and **video 2**, respectively. The evolution of the electric field orientation at the linearly polarized regions (Figs. 5 (a,c)) and of the vector \mathbf{s} at the circularly polarized regions (Figs. 5 (b,d)) are also included in each video.

4 4D optical skyrmionic textures

As pointed out in the introduction, a 3D polarization ellipse can be fully characterized by the positions of two indistinguishable points, \mathbf{p}_1 and \mathbf{p}_2 , over the unit sphere ($|\mathbf{p}_1| = |\mathbf{p}_2| = 1$). Different variants of this type of two-point construction exist: one proposed by Hannay [4] based on Majorana’s representation of spin systems; one referred to as the *Poincarana* representation that is naturally linked to geometric phase for nonparaxial fields [5]; and a more recent one [6] defined to satisfy certain statistical conditions. For all of them, the bisector of \mathbf{p}_1 and \mathbf{p}_2 is parallel to \mathbf{s} , the line joining \mathbf{p}_1 and \mathbf{p}_2 is parallel to the major axis of the ellipse, and the angular separation between \mathbf{p}_1 and \mathbf{p}_2 is a monotonic function of the ellipticity: the two points coincide for circular polarization, and they are antipodal for linear polarization. However, each construction encodes ellipticity in the angular separation of the points in a different manner.

For a field to span all 3D polarization states, each of the two points in any of these representations

must span the sphere independently, so that all combinations of the two point positions are represented. We then define a Skyrme number for this 4D space as

$$n_S = \iiint \Sigma_S dx dy dz dt, \quad (11)$$

where

$$\Sigma_S = \frac{1}{2(4\pi)^2} \sum_{i,j,k,l=1}^4 \epsilon_{ijkl} [\mathbf{p}_1 \cdot (\partial_i \mathbf{p}_1 \times \partial_j \mathbf{p}_1)] [\mathbf{p}_2 \cdot (\partial_k \mathbf{p}_2 \times \partial_l \mathbf{p}_2)] \quad (12)$$

is the Skyrme density, which corresponds to the Jacobian determinant between the coordinates in the abstract closed space (in this case the coordinates of the two points over the sphere) and the physical space (in this case space-time). Here ϵ_{ijkl} is the fourth-rank Levi-Civita tensor (which differs from zero only for the 24 terms for which all indices are different, out of the 64 in the sum), and ∂_i for $i = 1, 2, 3, 4$ represents a derivative in x, y, z, t , respectively. The factor of $1/(4\pi)^2$ is for normalizing the area of the sphere for each point, and the factor $1/2$ accounts for the indistinguishability of the two points. Due to the properties of the cross product, the 24 nonzero terms in the above expression reduce to the 6 terms corresponding to $(i, j, k, l) \rightarrow (x, y, z, t), (z, t, x, y), (x, z, y, t), (x, t, z, y), (z, y, x, t), (t, y, z, x)$, multiplied by a factor of 4.

This Skyrme number can be used for any of the three constructions mentioned earlier [4, 5, 6]. Here, we choose to use the Poincarana construction [5] (Fig. 6), where the midpoint between the points matches exactly \mathbf{s} . The Poincarana points are given by

$$\mathbf{p}_{1,2} = \mathbf{s} \pm \sqrt{1 - |\mathbf{s}|^2} \frac{\mathbf{a}}{|\mathbf{a}|}, \quad (13)$$

where \mathbf{a} is the major semi-axis of the polarization ellipse, which is obtained as $\mathbf{a} = \text{Re}(e^{-i\phi} \mathbf{E}/|\mathbf{E}|)$ with $\phi = \text{Arg}(\mathbf{E} \cdot \mathbf{E})/2$ [6]. We used this construction because it seems to lead to the simplest expressions for the Skyrme density in some cases.

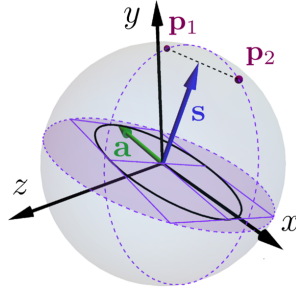


Figure 6: Poincarana representation construction: A fully polarized 3D polarization state is described by two indistinguishable points $\mathbf{p}_{1,2}$ on the unit sphere. The normalized spin density vector \mathbf{s} is the centroid of the two points, and the major semi-axis vector \mathbf{a} is parallel to the point separation.

For any α and β , the sign of Σ_S is uniform within each cell, A or B, but it is opposite between the two types of cell (due to the reversal in y of the polarization distribution). This sign also switches temporally every time Ωt is an integer multiple of $\pi/2$. We found that Σ_S is independent of z for any α and β , and it has periodic dependence on x for $\beta < \pi/4$ without changing sign (the sign depending only on y and t). Further, for $\beta = \pi/4$, we observed through numeric evaluation that Σ_S actually does not depend on x , and the long analytic expression for Σ_S greatly simplifies by setting $x = z = 0$, giving

$$\Sigma_S = \frac{k^3 \Omega}{\pi^2} \cos \alpha (\sqrt{2} - \cos \alpha) \cos \Omega t \sin^3 \Omega t \sin 2\kappa_y y. \quad (14)$$

This expression for Σ_S is plotted in Fig. 7(a) as a function of y and t for $\alpha = \beta = \pi/4$. For $\beta = \pi/4$, the Skyrme number inside a cell of type A or B can then be easily calculated analytically by integrating the Skyrme density in Eq. (14), giving the results $n_S = -1$ for cell A and $n_S = +1$ for cell B within the interval $\Omega t \in [0, \pi/2]$. We also verified numerically that $n_S = -(+)1$ in cell A(B) for several values of α and β . We then refer to the F3DP cells where $|n_S| = 1$ as *skyrmionic F3DP cells* (Fig. 7(b)). Other

versions of A and B displaced in x and/or z are also skyrmionic F3DP cells, since these displacements simply shift the relative phases between the components.

Note that, since Σ_S does not depend on z for any β , the Skyrme number accumulates linearly and indefinitely as the integration range in z increases. As a consequence, one can construct cells where $n_S = \pm 1$ that are not F3DP cells. There are also F3DP cells (containing each polarization state) whose volume is the same as that for A or B, but for which $n_S = 0$; we call these *nonskyrmionic F3DP cells*. An example corresponding to $\kappa_x x \in [0, \pi]$, $\kappa_y y \in [0, 2\pi]$ and $\kappa_z z \in [0, \pi/2]$ is shown in Fig. 7(c), which is composed of segments of cells of both types leading to cancellation of the Skyrme density contributions. More details about the construction of F3DP nonskyrmionic cells can be found in Section A.2 of the supplementary material.

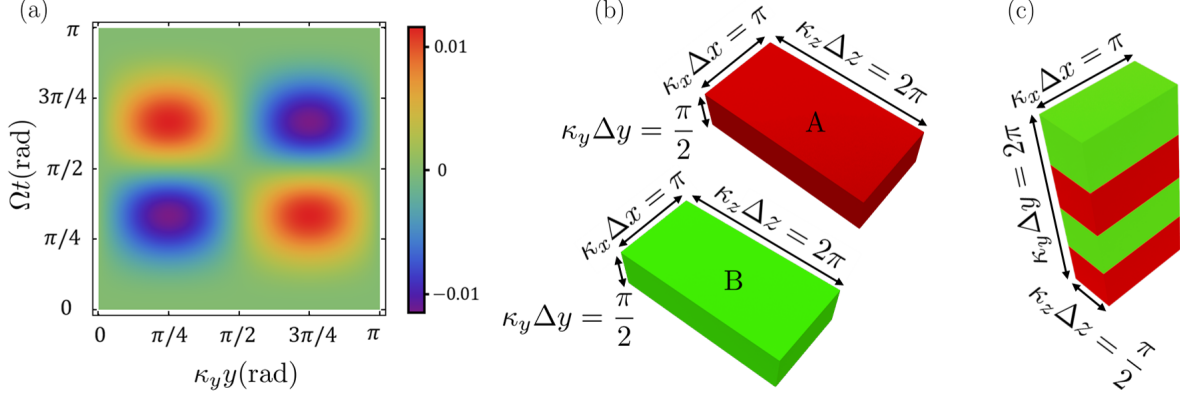


Figure 7: (a) Skyrme density for $\alpha = \beta = \pi/4$ in units of Ωk^3 . The Skyrme density beyond the plotted region is repeated. (b) F3DP skyrmionic cells. The Skyrme number is $- (+)1$ in cell A (B). (c) A F3DP nonskyrmionic cell that contains all 3D polarization ellipses and has the same volume as the F3DP skyrmionic cells, but has Skyrme number equal to 0.

5 Conclusions

We proposed a simple optical field that covers all possible states of nonparaxial polarization. This field is given by a superposition of five linearly-polarized plane waves whose amplitudes vary slowly in time. The polarization texture is periodic, and is composed of 4D skyrmionic spatio-temporal cells. The polarization distribution in each cell is described in terms of its “skeleton” given by the spatiotemporal manifolds of purely linear or circular polarization.

While the description in this work is theoretical, the experimental implementation of the field proposed here is probably not difficult to achieve, and this is currently underway in our group. The main challenge is most likely not the implementation of the field but its measurement. Current techniques for measuring nonparaxial polarization distributions rely on scanning a nanoparticle in order to measure one point at a time. Measuring this field would require scanning over four dimensions. We are currently working on an efficient measurement scheme that will allow sampling the 4D space more efficiently.

The simple forms proposed here are most likely not the only F3DP electromagnetic fields possible, although they might be the simplest ones. It would be interesting to investigate whether F3DP fields exist for which the Skyrme density does not change sign in space or time (making the skyrmionic structure more resilient to field perturbations). These fields might be periodic arrays of cells like the F3DP field here, or consist of a single cell occupying a theoretically infinite volume, in analogy to the 2D skyrmionic beams in [2]. Nevertheless, the constraints imposed by the Helmholtz equation and the divergence condition are stronger in the nonparaxial case than they are for paraxial beams.

Acknowledgement

This research received funding from the Agence Nationale de Recherche (ANR) through the project 3DPol, ANR-21-CE24-0014-01. D. M. acknowledges Ministerio de Universidades, Spain, Universidad Miguel Hernández and the European Union (Next generation EU fund) for a Margarita Salas grant from the program Ayudas para la Recualificación del Sistema Universitario Español.

References

- [1] M. Born and E. Wolf, *Principles of Optics: electromagnetic theory of propagation, interference and diffraction of light* (Cambridge University Press, 2001), pp. 25-33.
- [2] A.M. Beckley, T.G. Brown, and M.A. Alonso, “Full Poincaré beams,” *Opt. Express* **18**, 10777-10785 (2010).
- [3] N. Nagaosa and Y. Tokura, “Topological properties and dynamics of magnetic skyrmions,” *Nat. Nanotechnol.* **8**, 899-911 (2013).
- [4] J.H. Hannay, “The Majorana representation of polarization, and the Berry phase of light,” *J. Mod. Opt.* **45**, 1001-1008 (1998).
- [5] K.Y. Bliokh, M.A. Alonso and M.R. Dennis, “Geometric phases in 2D and 3D polarized fields: geometrical, dynamical, and topological aspects,” *Rep. Prog. Phys.* **82**, 122401 (2019).
- [6] M. A. Alonso, “Geometric descriptions for the polarization of nonparaxial light: a tutorial,” *arXiv:2008.02720v2* (2022).
- [7] S. Donati, L. Dominici, G. Dagvadorj, D. Ballarini, M. De Giorgi, A. Bramati, G. Gigli, Y. G. Rubo, M. H. Szymańska and D. Sanvitto, “Twist of generalized skyrmions and spin vortices in a polariton superfluid,” *Proc. Natl. Acad. Sci. U.S.A.* **113**, 14926–14931 (2016).
- [8] S. Gao, F. C. Speirits, F. Castellucci, S. Franke-Arnold, S.M. Barnett and J.B. Götte, “Paraxial skyrmionic beams,” *Phys. Rev. A* **102**, 053513 (2020).
- [9] S. Tsesses, E. Ostrovsky, K. Cohen, B. Gjonaj, N.H. Lindner, and G. Bartal, “Optical skyrmion lattice in evanescent electromagnetic fields,” *Science* **361**, 993-996 (2018).
- [10] H. Ge, X.-Y. Xu, L. Liu, R. Xu, Z.-K. Lin, S.-Y. Yu, M. Bao, J.-H. Jiang, M.-H. Lu, and Y.-F. Chen, “Observation of Acoustic Skyrmions,” *Phys. Rev. Lett.* **127**, 144502 (2021).
- [11] R. D. Muelas-Hurtado, K. Volke-Sepulveda, J. L. Ealo, F. Nori, M. A. Alonso, K. Y. Bliokh, E. Brasselet, “Observation of polarization singularities and topological textures in sound waves,” *Phys. Rev. Lett.* **129**, 204301 (2022).
- [12] L. Du, A. Yang, A. V. Zayats, and X. Yuan, “Deep-subwavelength features of photonic skyrmions in a confined electromagnetic field with orbital angular momentum,” *Nat. Phys.* **15**, 650-654 (2019).
- [13] R. Gutiérrez-Cuevas and E. Pisanty, “Optical polarization skyrmionic fields in free space,” *J. Opt.* **23**, 024004 (2021).
- [14] D. Sugic, R. Droop, E. Otte, D. Ehrmanntraut, F. Nori, J. Ruostekoski, C. Denz, and M.R. Dennis, “Particle-like topologies in light,” *Nat. Commun.* **12**, 6785 (2021).
- [15] M.V. Berry and M.R. Dennis, “Polarization singularities in isotropic random vector waves,” *Proc. R. Soc. A* **457**, 141-55 (2001).
- [16] K.Y. Bliokh and F. Nori, “Transverse and longitudinal angular momenta of light,” *Phys. Rep.* **592**, 1-38 (2015).
- [17] A. Aiello, P. Banzer, M. Neugebauer, and G. Leuchs, “From transverse angular momentum to photonic wheels,” *Nat. Photon.* **9**, 789-795 (2015).

A Supplementary material

We include in the supplementary material details about the L-lines, C-lines, and of the nonskyrmionic F3DP cells.

A.1 Skeleton

In this section, we provide details of the derivation of the L-lines, and equations for the C-lines, the normalized spin density vector \mathbf{s} , and the topological transitions that the C-lines undergo. We also study the evolution of the L-lines and C-lines for $\beta < \pi/4$, in particular for the case $\alpha = \tilde{\alpha}$ and $\beta = \tilde{\beta}$, shown in Fig. 8.

A.1.1 The L-lines within cell A

Here, we describe how to obtain the L-lines for the field defined in Eq. (9). As mentioned in the main text, for $\Omega t = 0$, the field has a polarization state \mathbf{y} , which means that the 3D space itself is an L-volume. For $\Omega t = \pi/2$, on the other hand, only the components \mathbf{p} and \mathbf{m} survive. If, in addition, $\kappa_y y = n\pi/2$ ($n \in \mathbb{Z}$), then only one linear polarization component remains, so this condition defines planes of constant y with \mathbf{p} (for $\kappa_y y = n\pi$) or \mathbf{m} (for $\kappa_y y = (2n+1)\pi/2$) polarization state. Conversely, for $\kappa_y y \neq n\pi/2$, the phase between the \mathbf{p} and \mathbf{m} components must be $n\pi$ for the state to be linear, which defines a set of L-planes $x = n\pi/(2\kappa_x)$.

Within the intermediate interval $\Omega t \in (0, \pi/2)$ we find L-lines. The first subset of L-lines is deduced for $\kappa_y y = n\pi/2$. Under this spatial constraint, only two polarization components survive (\mathbf{y} and \mathbf{p} or \mathbf{y} and \mathbf{m}), and in order to have linearly polarized light, the relative phase between these components must be $n\pi$, which, together with the condition $\kappa_y y = n\pi/2$, defines a set of L-lines that lie on the planes $y = 0$ and $y = \lambda/(4 \sin \alpha)$ in the F3DP cell A. The second set of L-lines is deduced for $\kappa_y y \neq n\pi/2$ (i.e., when the three linear polarization components survive), imposing that the two relative phases between the three linear polarization components must be integer multiples of π .

A.1.2 The C-lines within cell A

The equations defining the C-lines for the field defined in Eq. (9) can be found from the condition $\mathbf{E} \cdot \mathbf{E} = 0$, whose real and imaginary parts lead to

$$\cos^2 \Omega t \cos 2\kappa_z z + \sin^2 \Omega t (\cos 2\kappa_x x - \cos 2\beta \sin 2\kappa_y y) = 0, \quad (15a)$$

$$\cos^2 \Omega t \sin 2\kappa_z z - \sin^2 \Omega t \cos 2\kappa_y y \sin 2\kappa_x x = 0. \quad (15b)$$

Using $\mathbf{s} = \text{Im}(\mathbf{E}^* \times \mathbf{E})/|\mathbf{E}|^2$, we obtain the normalized spin density vector \mathbf{s} for the field defined in Eq. (9):

$$\mathbf{s} = \frac{1}{|\mathbf{E}|^2} \begin{pmatrix} -\sin 2\Omega t \sin \beta [\cos \kappa_y y \sin (\kappa_z z + \kappa_x x) + \sin \kappa_y y \sin (\kappa_z z - \kappa_x x)] \\ -\sin^2 \Omega t \sin 2\beta \sin 2\kappa_x x \sin 2\kappa_y y \\ \sin 2\Omega t \cos \beta [\cos \kappa_y y \sin (\kappa_z z + \kappa_x x) - \sin \kappa_y y \sin (\kappa_z z - \kappa_x x)] \end{pmatrix}, \quad (16)$$

where

$$|\mathbf{E}|^2 = 1 - \sin^2 \Omega t \cos 2\beta \cos (2\kappa_x x) \sin (2\kappa_y y) \quad (17)$$

is the field intensity.

For $\beta < \pi/4$, we observed for multiple values of β that the C-lines in the F3DP cell A always appear as points at $x = \pi/(2\kappa_x)$, $y = \pi/(4\kappa_y)$, $z = \pi/\kappa_z$, and $x = \pi/(2\kappa_x)$, $y = \pi/(4\kappa_y)$, $z = 0$. (It is only for $\beta = \pi/4$ that they appear as lines and they also appear at other regions.) Evaluating \mathbf{s} at these spatial coordinates reveals that \mathbf{s} points in the $\pm z$ direction at these points, as can be seen for $\alpha = \tilde{\alpha}$ and $\beta = \tilde{\beta}$ in Fig. 8 and on the sphere in Fig. 5(d). Setting $|\mathbf{s}| = 1$ (which implies circular polarization) at these points, we arrive at the expression

$$\Omega t_C = \arccos \left(\frac{\cos \beta}{\sqrt{1 + \frac{\cos 2\beta}{2}}} \right) \quad (18)$$

for the time t_C when the C-lines appear: $\Omega t_C = \pi/4$ for $\beta = \pi/4$ (Fig. 4) and $\Omega t_C = 0.6331$ for $\beta = \tilde{\beta}$ (Fig. 8). As mentioned in the main text, we observed a topological transition at $\Omega t_{T1} = \pi/4$ for any β . At a given time t_{T2} , there is another topological transition for the C-lines. We observed that there are two helical C-lines inside the F3DP cell A meeting at the points $x = 0, y = \pi/(4\kappa_y)$ and $z = \pi/(2\kappa_z)$, and $x = 0, y = \pi/(4\kappa_y)$ and $z = \pi/\kappa_z$ for any β . Evaluating the vector \mathbf{s} in these coordinates we found that the vector \mathbf{s} points along $+x$ ($-x$) for any β at these points. Imposing that $|\mathbf{s}| = 1$, we arrive at

$$\Omega t_{T2} = \arccos \left(\frac{\sin \beta}{\sqrt{1 - \frac{\cos 2\beta}{2}}} \right). \quad (19)$$

The topological transition is noticeable from the unit sphere in Fig. 5(d). It occurs when \mathbf{s} points along x and $-x$ and it is a very fast transition. For $\beta = \tilde{\beta}$, $\Omega t_{T2} = 1.2094$, while for $\beta = \pi/4$, $\Omega t_{T2} = \pi/4$. As pointed out in the main text, for $\beta = \pi/4$, the topological transitions and the appearance of the C-lines occur at the same instant $\Omega t_C = \Omega t_{T1} = \Omega t_{T2} = \pi/4$. However, as β decreases, the instants t_C and t_{T2} move away from each other in time while Ωt_{T1} remains at $\pi/4$ as shown in the plot in Fig. 9.

Figure 8 shows the L-lines, the C-lines and the \mathbf{s} vector inside the F3DP cell A for $\alpha = \tilde{\alpha}$ and $\beta = \tilde{\beta}$. Here, the C-lines appear as points at $\Omega t_C = 0.6331$. The plot for $\Omega t = \pi/4 - \pi/50$ in Fig. 8 shows that shortly after t_C , the C-lines become small closed loops that spill into neighboring F3DP cells (as can be deduced from the brick-like structure in Fig. 3(b)). These loops grow until, right before $\Omega t = \Omega t_{T1} = \pi/4$, segments of them almost lie on the $y = 0$ plane while others almost lie on the $y = \lambda/(4 \sin \alpha)$ plane. At the topological transition at $\Omega t_{T1} = \pi/4$, pairs of C-lines segments lying on the same plane of constant y get linked by straight C-lines. These straight lines come from closed C-lines loops in the upper and lower F3DP cells. Right after $\Omega t = \pi/4$, the segments almost lying on the $y = 0$ and $y = \lambda/(4 \sin \alpha)$ surfaces before $\Omega t = \pi/4$ disappear from the cell; they move to the F3DP cells above and below to form the same structure they form in A but displaced and reflected along y . This structure consists of two tangled helical C-lines winding around each other. At the second topological transition at Ωt_{T2} , the two helical lines meet at two points, and right after t_{T2} , the C-line segments within $x > 0$ combine to form a new C-line, and the same for $x < 0$, so there are now two untangled helical C-lines. After t_{T2} , the C-lines behave as they did for $\beta = \pi/4$: as Ωt increases the lines straighten gradually until they become straight for $\Omega t = \pi/2$, when the ellipses are constrained to the xz plane, and pure transverse spin appears.

A.2 F3DP nonskyrmionic cells

In section 4, we reported the existence of F3DP cells where $n_S = 0$. We show in Fig. 10 examples of regions containing all 3D polarization ellipses where $n_S = 0$. The regions in (a) and (b) are constructed as follows: First, we take one or more regions in A that sum up to half of the A volume by slicing A along z . Then, we take the regions in B containing all the polarization states that are not in the chosen A regions (i.e., the regions in B that are not a displacement of the A regions by $\pi/2$ in $\kappa_x x$, $\kappa_y y$ and $\kappa_z z$). Since Σ_S does not depend on z , n_S grows linearly with z , and thus the total n_S is $-1/2$ ($+1/2$) in the A (B) sub-regions, so their Skyrme numbers always cancel. A simple example is depicted in Fig. 10(a), where we took the second half of cell A. We can choose the A volumes to be split into two parts as shown in Fig. 10(b). Following the stacking rules to reproduce the field in subsection 3.1, one realizes that the cell in Fig. 7(c) ($\kappa_x x \in [0, \pi]$, $\kappa_y y \in [0, 2\pi]$ and $\kappa_z z \in [0, \pi/2]$), which is also shown in Fig. 10(c), can be built from Fig. 10(b), but now all the parts of the cell are connected forming a cuboidal F3DP nonskyrmionic cell.

A.3 Videos

We show the evolution of the L-lines, C-lines and normalized spin density vector \mathbf{s} inside the F3DP cell A for $\alpha = \beta = \pi/4$ (**video 1**) and for $\alpha = \tilde{\alpha}$ and $\beta = \tilde{\beta}$ (**video 2**). The evolution of the electric field orientation at the regions of linear polarization and of the \mathbf{s} vector at the C-lines over the unit sphere is included.

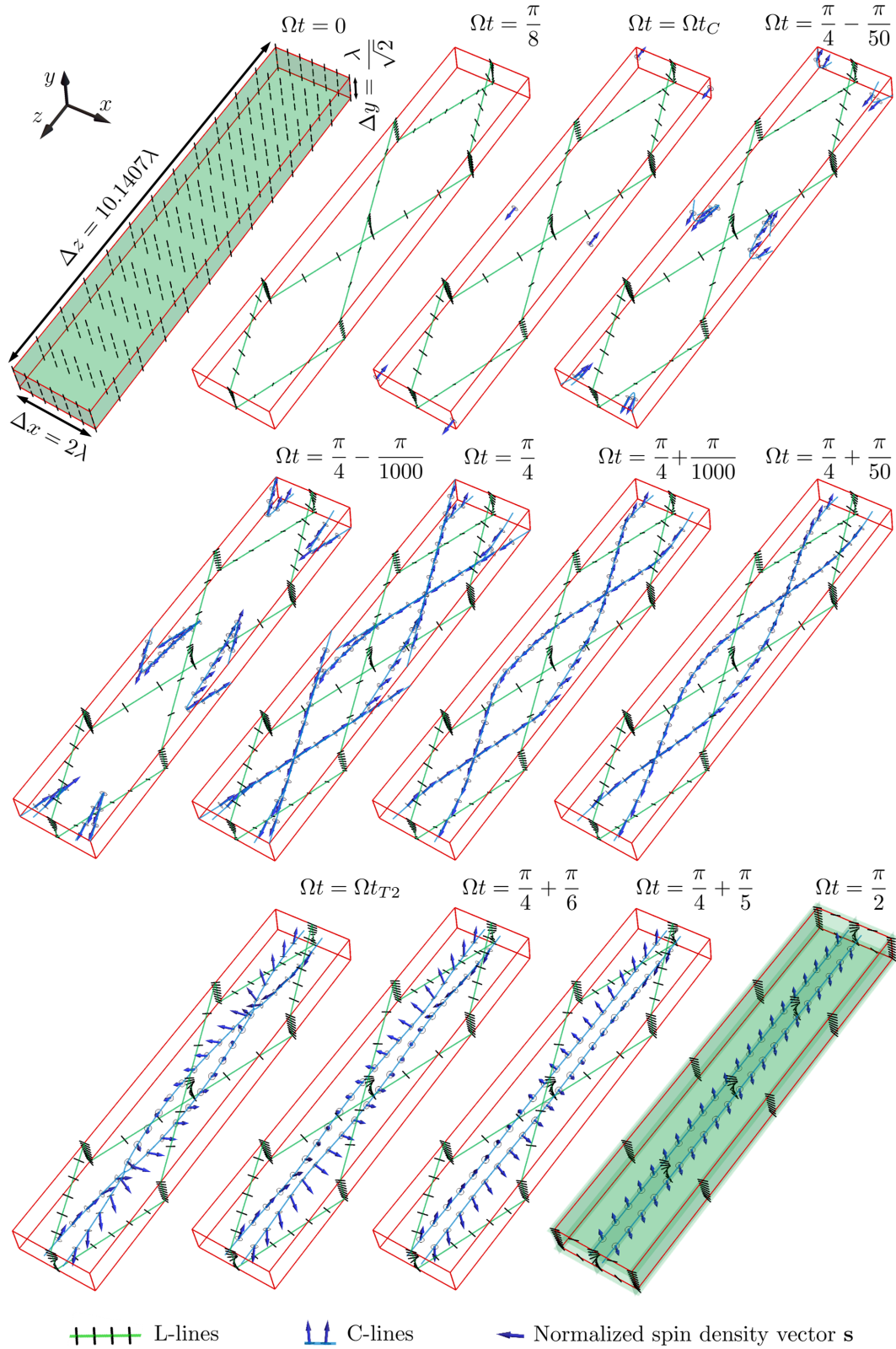


Figure 8: Temporal evolution of the L-lines and C-lines inside the F3DP cell A for $\alpha = \tilde{\alpha}$ and $\beta = \tilde{\beta}$ (for which the dimensions of the F3DP cell in x and y are twice as large as for the cell corresponding to $\alpha = \beta = \pi/4$). The polarization ellipses are plotted for the C-lines and L-lines, and the normalized spin density vector is plotted for the C-lines. At $\Omega t_C = 0.6331$, the C-lines appear as points. There are two topological transitions, occurring at $\Omega t_{T1} = \pi/4$ and at $\Omega t_{T2} = 1.2094$.

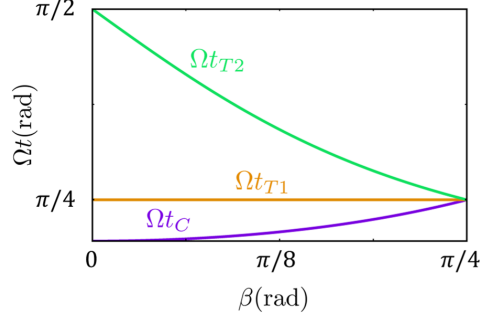


Figure 9: Dependence on β of the time t_C when the C-lines appear, and of the topological transition times t_{T1} and t_{T2} .

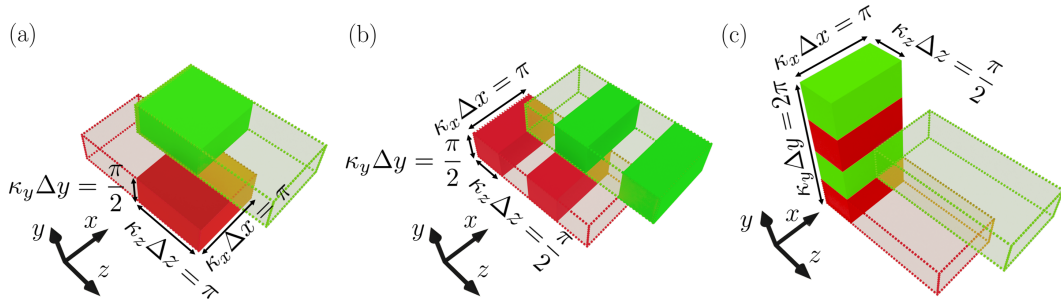


Figure 10: Nonskyrmionic F3DP regions. The unit cell of the polarization structure of the field has been depicted as two dashed cuboids to better visualize the nonskyrmionic F3DP regions.